Nanoscale

PAPER

View Article Online
View Journal | View Issue



Cite this: *Nanoscale*, 2025, **17**, 3221

# Impact of different 2D materials on the efficacy of photothermal and photodynamic therapy in 3D-bioprinted breast cancer

Giordano Perini,[a,b] Antonio Minopoli,[a,b] Dario Zambrano,[c] Lishan Cui,[a] Valeria Ferrara,[a,b] Caterina Perfili,[a,b] Giulia Artemi,[d] Marco De Spirito,[a,b] Valentina Palmieri, *[a,b,d] Andreas Rosenkranz[e,c] and Massimiliano Papi *[a,b]

The convergence of nanotechnology and tissue engineering has paved the way for innovative cancer treatments that leverage the unique light absorption properties of nanomaterials. Indeed, photothermal therapy (PTT) and photodynamic therapy (PDT) utilize nanomaterials to convert near-infrared light into therapeutic energy for cancer treatment. This study focuses on the application of poly(lactic-*co*-glycolic acid) (PLGA) scaffolds, enhanced by graphene oxide, $Ti_3C_2T_x$ MXene, and $TiS_2$ transition metal dichalcogenides for PDT and PTT treatments evaluated within 3D-bioprinted breast cancers. Our scaffolds were designed to exploit the photothermal conversion efficiency and capability to generate reactive oxygen species (ROS) to compare the specific features of each 2D material. We demonstrated a reduction in tumor viability under scaffold irradiation, along with the exploration of biological responses to damage such as autophagy and pyroptosis, verifying that these scaffolds can differentially induce these processes depending on the light responsiveness of each material. The integration of these materials within 3D-printed scaffolds does not only enhance the therapeutic efficacy of PTT and PDT, but also offers a precise method to control the cellular environment after therapy, *i.e.* tissue regeneration and antibacterial effects, providing insights into the potential for these technologies to be adapted for personalized medicine for breast cancer treatment and reconstruction.

Received 29th November 2024,
Accepted 13th December 2024

DOI: 10.1039/d4nr05026f

rsc.li/nanoscale



## Introduction

The integration of cutting-edge nanomaterials and innovative techniques has unveiled a promising avenue for tissue engineering and cancer therapy.[1] Photothermal therapy (PTT) and photodynamic therapy (PDT) have emerged as interesting approaches, making use of the unique properties of nanomaterials to revolutionize cancer treatment.[2,3] Among nanomaterials, graphene oxide (GO), MXenes (MX), and transition metal dichalcogenides (TMDCs) represent versatile 2D platforms for the development of highly effective and targeted cancer therapies, though the PDT/PTT efficiencies of these materials have not been compared.[4–7]

GO is a derivative of graphene, characterized by its layered structure and functional groups such as hydroxyl, carboxyl, and epoxy, which impart hydrophilicity and chemical reactivity. These functional groups enable GO to interact with various biological molecules, making it useful in biomedical applications such as drug delivery, biosensing and 3D scaffold production.[8–10] MXenes, composed of transition metals like titanium or molybdenum combined with carbon or nitrogen, exhibit a unique 2D structure with high electrical conductivity and hydrophilicity due to surface terminations like hydroxyl or oxygen groups.[11] TMDCs are layered materials with a structure akin to graphene, but with intrinsic semiconducting properties due to the presence of metal and chalcogen atoms.[12] TMDCs have strong light–matter interactions, making them promising candidates for optoelectronic devices, photodetectors, and biomedical imaging. Their biocompatibility and ease of functionalization further enhance their potential in medical diagnostics and therapeutic applications. The ability of GO, MXenes, and TMDCs to absorb and convert near-infrared (NIR) light into therapeutic energy forms the cornerstone of their utility in PTT. These 2D nanomaterials exhibit remarkable photothermal conversion efficiencies, generating localized hyperthermia upon NIR irradiation.[13–15] A controlled and

[a]*Dipartimento di Neuroscienze, Università Cattolica del Sacro Cuore, Largo Francesco Vito 1, 00168 Rome, Italy. E-mail: massimiliano.papi@unicatt.it*
[b]*Fondazione Policlinico Universitario A. Gemelli IRCSS, 00168 Rome, Italy*
[c]*Department of Chemical Engineering, Biotechnology and Materials (FCFM), Universidad de Chile, Santiago, Chile*
[d]*Istituto dei Sistemi Complessi, CNR, Via dei Taurini 19, 00185 Rome, Italy. E-mail: valentina.palmieri@cnr.it*
[e]*ANID – Millennium Science Initiative Program, Millennium Nuclei of Advanced MXenes for Sustainable Applications (AMXSA), Santiago, Chile*

site-specific temperature increase within the tumor microenvironment has proven to be highly effective to induce the death of cancer cells, while ensuring that the adjacent healthy tissue remains unaffected.[16] Consequently, the integration of GO, MX, and TMDCs in PTT has opened new avenues for non-invasive, precise, and minimally cytotoxic cancer therapy.[17] Beyond PTT, the multi-faceted capabilities of nanomaterials extend to PDT, where they serve as carriers for photosensitizers or act as photosensitizing agents.[18] GO, MX, and TMDCs can induce the generation of reactive oxygen species (ROS) upon exposure to light, generating oxidative stress and cell death.[5,13,19,20] The dual-mode therapy, incorporating both PTT and PDT, represents a potent strategy for synergistic cancer treatment, effectively targeting primary tumors as well as metastatic lesions.[5,13] Several research papers have been focused on PTT and PDT clinical translation, including efforts toward the treatment of breast cancer, the most prevalent form of cancer worldwide.[21] Reconstructing soft tissue after breast cancer treatment is crucial, as substantial evidence supports its benefits in enhancing both physical and psychological health. Additive manufacturing methods enable the creation of custom implants featuring intricate, porous designs with high precision and consistency. The ability to reliably control the scaffold's architecture is crucial, as the internal configuration significantly influences cell infiltration, tissue structuring, and ultimately, homeostasis.[22] Indeed, the timing of permanent reconstruction is crucial because in the case of radiation therapy, this will impact both the immediate and long-term tissue regeneration.[23] Furthermore, implant interaction with cells might even influence cancer recurrence.[24]

In this study, we assessed the potential of 3D-printed scaffolds constructed from poly(lactic-*co*-glycolic acid) (PLGA) blended with GO, $Ti_3C_2T_x$ (MX), or TiS,[25] serving as catalysts for a dual-mode photothermal and photodynamic effect.[26] The core of our investigation revolves around the creation of a tumor model using breast cancer cells and Matrigel bioprinted in contact with 3D-printed nanomaterial-enriched scaffolds.[27] Subsequently, we subjected these scaffolds to irradiation with an 808 nm NIR laser, and elucidated the impact on tumor viability. Our findings underscored the striking efficiency of this approach in tumor destruction, largely attributed to the unique properties and interactions of GO, MX, and TMDCs within the scaffold matrix. Notably, the nature of these nanomaterials was directly related to the respective ROS production and cell death pathways. We also quantified the antibacterial properties of the scaffolds, with or without NIR irradiation, and described the bioconductivity that the scaffolds provide towards healthy fibroblasts, resembling tissue regeneration after *in vivo* therapy. Finally, since the key point of cancer treatment based on photoadsorbers is the activation of patient immune response, we quantified the migration of human monocytes towards treated cancers and demonstrated marked activation of the immune system. This work holds profound implications to tailor and optimize PTT and PDT aspects *in vivo*, emphasizing the crucial role of these materials in shaping the treatment's efficacy on patient's needs in breast cancer management.[3,4,28]

# Materials and methods

## Materials

Following the Hummers approach,[29] graphite was oxidized using $KMnO_4$ and $NaNO_3$ in concentrated sulfuric acid. To adjust a certain oxidation degree, the graphite/$KMnO_4$ mass ratio was properly adjusted, followed by annealing of the GO solution at 50 °C for 30 minutes. TMDCs ($TiS_2$ nano-sheets) were commercially purchased from Sigma Aldrich and used without any further pre-treatment. To generate multi-layer $Ti_3C_2T_x$ nano-sheets (MX), 5 g of MAX phase precursor $Ti_3AlC_2$ (Forsman Scientific Co. Ltd, Beijing, China) was submerged in an aqueous HF solution (50 ml of hydrofluoric acid with a concentration of about 40%). The solution was kept under continuous magnetic stirring at a constant speed of 60 rpm for one day. After the chemical etching treatment, the solution was centrifuged for 5 minutes at 3500 rpm before adjusting the pH to neutral by several washing cycles using deionized water. Subsequent filtering was performed by vacuum-assisted filtration using a water circulating vacuum pump with polyether-sulfone filter membranes. Finally, the solution was stored in a fridge for 8 h at a temperature of −10 °C before being freeze-dried at −60 °C and a pressure below 30 Pa for one day. The quality, structure and morphology of the used nanomaterials were assessed by electron microscopy, X-ray diffraction (XRD) and Raman spectroscopy. Regarding electron microscopy, the GO nano-sheets were imaged by transmission electron microscopy (TEM, Tecnai F20, FEI) using an acceleration voltage of 200 keV. $Ti_3C_2T_x$ and $TiS_2$ nano-sheets were characterized using a field-emission scanning electron microscope (FE-SEM, Σigma Carl Zeiss), operating at an acceleration voltage of 20 keV. The overall surface chemistry was characterized by X-ray diffraction (XRD) using a powder diffractometer (PANalytical Empyrean) operating in the Bragg–Brentano configuration at 40 kV and 40 mA with CuKα irradiation. An angular step size of 0.026° and a dwell time of 1396.89 s for each measuring point have been chosen. Raman spectroscopy (LabRAM HR Evolution) was performed for all initial powders to assess their overall chemistry. In this regard, Raman spectra were obtained in backscattering geometry using an excitation wavelength of 532 nm. The spectra were recorded in the spectral range from 80 to 1000 $cm^{-1}$ with an acquisition time of 128 s per spectrum and a spectral resolution of 3 $cm^{-1}$ using a grating with a resolution of 1800 l $mm^{-1}$.

## Cell culture

HCC1806 human breast cancer cells, human fibroblasts, human bone marrow mesenchymal stem cells (hBMSCs) and THP-1 human monocytes were purchased from the American Type Culture Collection (ATCC). Breast cancer cells and THP-1 were maintained in RPMI medium (Sigma-Aldrich) supplemented with 10% fetal bovine serum (FBS, EuroClone), 2% penicillin–streptomycin (Sigma-Aldrich) and 2% L-glutamine (Sigma-Aldrich). Human fibroblasts and hBMSCs were cultured in DMEM (Sigma-Aldrich) supplemented with 10% FBS (EuroClone) and 2% penicillin–streptomycin (Sigma-Aldrich).

 

The cells were kept in T75 flasks (Corning) at 37 °C under 5% $CO_2$ for further treatments.

### 3D-printing of scaffolds

3D-printing of the PLGA, PLGA–GO, PLGA–MX and PLGA–TMDC scaffolds was performed with a BIO X 3D bioprinter (Cellink). PLGA flakes (Rimless Industry) and the respective nanomaterials in powder form were mixed by keeping the nanomaterials fixed at 2% w/w in dichloromethane (Carlo Erba) with respect to PLGA. The mixture was agitated overnight, followed by air drying. The produced films were cut into small pieces and subsequently transferred into a thermoplastic print head (Cellink) having a heating capacity of up to 250 °C. The structure of the scaffolds was designed using modeled 3D computer graphics and a computer-aided design (CAD) software (Rhinoceros software, Robert McNeel & Associates). The scaffolds were printed *via* an extrusion-based technique by adjusting a print head temperature of 185 °C and a print bed temperature of 65 °C. The extrusion pressure was set at 40 kPa, with a pre-flow of 20 ms and a speed of 22 mm $s^{-1}$.

### 3D-bioprinting of breast cancer

Three-dimensional breast tumor models have been prepared from breast cancer cells. Tumor models were produced *via* 3D-bioprinting. As a bioprinting strategy, droplet printing was used with BIO X (Cellink). For this purpose, $2 \times 10^6$ cells per mL were mixed with Matrigel (Corning) in a syringe with a 1 : 10 ratio of cells and bioink, respectively. HCC1806 cells mixed with the hydrogel were loaded in a temperature-controlled bioprinting cartridge (Cellink) set at 4 °C. Tumor domes were printed in 48-well plates (Corning) at an extrusion rate of 5. 3D-bioprinted models were then crosslinked at 37 °C and the wells were filled with the culture medium. Tumor models were then incubated at 37 °C under 5% $CO_2$ for further treatments. We monitored the growth of the bioprinted models using a Cytation 3 Cell Imaging Multi-Mode Reader (BioTek). We collected bright-field data on a time span of 14 days and processed them using the FIJI software.

### Near-infrared radiation

An NIR laser (LaserEver) with a wavelength of 808 nm was used to perform PTT/PDT on the cells. Initially, the laser was characterized by evaluating the laser power at every current intensity using a power meter. The spot of the laser had a diameter of 0.8 cm. The power density was evaluated by normalizing the laser power to the spot area. The scaffolds were put in a 48-well plate (Corning) and covered with the culture medium. Then, they were irradiated for 3 minutes at different power densities to achieve the same final temperature. It is important to note that the necessary power density to reach the target temperature was dependent on the material. In this regard, the PLGA scaffolds enriched with GO, MXenes and TMDCs were irradiated using currents of 1.005, 1.042 and 0.998 A and power densities of 0.71, 0.85 and 0.68 W $cm^{-2}$, respectively. The energy density for the scaffolds was 127.8, 153 and 122.4 J $cm^{-2}$, respectively. The temperature increase was monitored using a thermal camera (Optris) focused on the well.

### Thermodynamic simulation

To infer the temperature distribution in 3D-bioprinted models, we numerically solved the heat-conduction equation (Fick's law) under local laser stimuli by using the finite element method (FEM) in COMSOL Multiphysics. The simulation framework consisted of a hydrogel-based dome ($a_x$ = 3 mm, $a_y$ = 3 mm, and $a_z$ = 2 mm) lying on a PLGA–GO disk (radius = 5 mm, thickness = 0.3 mm, density = 1.3 g $cm^{-3}$, and thermal conductivity = 1 W $m^{-1}$ $K^{-1}$)[30,31] and surrounded by a water layer of thickness 5 mm. To emulate the hydrogel environment, we defined a fluid-like medium with a thermal conductivity of 0.57 W $m^{-1}$ $K^{-1}$, a density of 1.1 g $cm^{-3}$ and a viscosity of 1 kPa. The deposited beam power on the scaffold was set at 0.7 W $cm^{-2}$ with a Gaussian beam profile ($\sigma$ = 4 mm), according to the experimental conditions for PLGA–GO irradiation. The initial temperature of the system was set at 25 °C, whereas the remaining domains/interfaces could freely transfer the heat. The meshing was adaptive and chosen to be finer close to the dome.

### Cell viability

To test the biocompatibility and cell adhesion of the 3D-printed scaffolds on a 2D culture model, human breast cancer cells and human fibroblasts were seeded on the scaffolds in 48-well plates at a seeding density of $3 \times 10^4$ cells per well. After incubation, the cells were stained using a live/dead assay. Briefly, calcein-AM (Invitrogen), capable of staining live cells, and propidium iodide (PI, Sigma-Aldrich), capable of staining dead cells, were added to the culture medium at a final concentration of 5 μM. After 20 minutes of incubation at 37 °C under 5% $CO_2$, the fluorescence intensity and fluorescence images of the two probes were obtained using a Cytation 3 Cell Imaging Multi-Mode Reader (BioTek). The ratio between live and dead cells was used to evaluate viability on 2D cultures. The results were expressed as % of control cells. Adhesion was evaluated by counting the number of viable cells through fluorescence microscopy by acquiring representative images.

To evaluate the potential toxicity of the 3D-printed scaffolds, cell viability tests were conducted using CellTiter-Glo 3D (Promega). Prior to bioprinting the tumor mass, the breast cancer cells were printed onto 48-well plates at a concentration of $2 \times 10^6$ cells per mL. One day after NIR treatment, CellTiter-Glo 3D was added to each well with a volume equal to the culture medium and shaken for 5 minutes in an orbital shaker to induce cell lysis. The plates were incubated at room temperature for 25 minutes before recording luminescence using a Cytation 3 Cell Imaging Multi-Mode Reader. Viability was expressed as the percentage of untreated (control) cells.

### Production of ROS

To evaluate the direct photodynamic conversion effect of the scaffolds without cells, the ROS-ID detection kit (Enzo Life Sciences) was utilized. This kit allows the measurement of the

total ROS levels as well as specific detection of superoxide production. It includes two main components: the oxidative stress detection reagent (green) for broad-spectrum ROS detection and the superoxide detection reagent (orange) for superoxide-specific analysis. The green probe reacts with various reactive species, producing a green fluorescence signal that indicates the overall ROS levels, while the orange probe, a cell-permeable dye, selectively interacts with superoxide to generate an orange fluorescence signal. In our experiments, the scaffolds were exposed to NIR irradiation for 3 minutes. The scaffolds were submerged in the detection solution throughout the irradiation process. Following NIR exposure, the 3D-printed constructs were incubated at 37 °C under 5% $CO_2$ for 1 hour. Fluorescence intensities were then measured in the supernatant using a Cytation 3 Cell Imaging Multi-Mode Reader. Readings were taken at 490 nm excitation with 525 nm emission for the green probe and 550 nm excitation with 620 nm emission for the orange probe.

To assess the presence of ROS following NIR exposure on bioprinted models over the scaffolds, we utilized a fluorinated derivative of 2′,7′-dichlorofluorescein known as $H_2$DCFDA (Sigma-Aldrich). This specific probe remains non-fluorescent until intracellular esterases remove the acetate groups and induce oxidation within cellular environments. Consequently, the occurrence of oxidation was monitored by observing the increase in fluorescence intensity. In our experiments, 3D-bioprinted breast cancer models that were put in contact with the scaffolds were subjected to NIR irradiation (808 nm) for a duration of 3 minutes. Following the NIR treatment, we incubated the scaffolds at 37 °C under 5% $CO_2$. We then replaced the culture medium with PBS containing 10 μM $H_2$DCFDA. The tumor models were allowed to incubate for 30 minutes at 37 °C under 5% $CO_2$. Subsequently, we removed the $H_2$DCFDA-containing PBS and replaced it with complete medium. To quantify the fluorescence intensity of $H_2$DCFDA, we employed a Cytation 3 Cell Imaging Multi-Mode Reader, exciting the sample at 495 nm and recording the emission at 528 nm. Our findings were expressed with respect to viable cells. A computational model was also developed using COMSOL Multiphysics to simulate ROS diffusion and consumption within a 3D-bioprinted breast cancer model exposed to NIR radiation. ROS transport was modeled using the Transport of Diluted Species module, incorporating diffusion to reflect cellular antioxidant defenses. Boundary conditions included no-flux constraints at scaffold edges and ROS decay in the extracellular environment. Simulations provided spatial and temporal ROS concentration profiles, with sensitivity analyses performed to evaluate the impact of antioxidant efficiency.

### Migration of immune cells

To test the effect of NIR on the migration of immune cells, NIR therapy was carried out on bioprinted breast cancer models. After the treatment, the supernatant of bioprinted models was collected, centrifuged and transferred to the lower chamber of a transwell system at a final volume of 600 μL. THP-1 cells were seeded on the upper chamber of the transwell system (5 μm pore size) at a seeding density of $10^5$ cells per mL. After 24 h of incubation, calcein was added to the lower and the upper chambers at a final concentration of 5 μM, and the multiwell was incubated for 30 min at 37 °C under 5% $CO_2$. Following the incubation, the fluorescence intensity of calcein was recorded on both sides of the transwell by exciting at 480 nm and recording the emission at 535 nm. To quantify the migration efficiency, we first evaluated the relative fluorescence (RF), expressed as the ratio between the fluorescence intensities of migrated and not migrated cells. We then measured the efficiency as $RF_{NIR}/RF_{No\ NIR}$.

### Autophagy measurement

Autophagy after NIR exposure was evaluated with the autophagy assay kit (Sigma-Aldrich), which exploits a fluorescent marker of the formed autophagosome. Briefly, the culture medium was removed and the autophagosome detection reagent working solution was added according to the manufacturer's instructions. Tumor models were incubated at 37 °C under 5% $CO_2$ for 45 minutes. The samples were then washed with wash buffer. Subsequently, the fluorescence intensity was recorded with a Cytation 3 Cell Imaging Multi-Mode Reader by exciting at 360 nm and recording the emission at 520 nm.

### Pyroptosis

To test pyroptosis induced by PTT/PDT, we measured the release of gasdermin D (GSDMD) from the cells after NIR exposure using the GSDMD ELISA kit (Abcam) following the manufacturer's instructions. Briefly, 50 μL of the supernatant from the treated cells was mixed with 50 μL of GSDMD antibody and incubated for 1 hour at room temperature on a plate shaker at 400 rpm. The mixture was washed 3 times with the respective wash buffer. Then, absorbance was recorded at 450 nm.

### Antibacterial activity

The antibacterial properties of the PLGA, PLGA–GO, PLGA–MX and PLGA–TMDC scaffolds were tested against *Escherichia coli* (*E. coli*) ATCC 25922 and *Staphylococcus aureus* (*S. aureus*) ATCC 29213. Each strain was inoculated in 10 mL of Lennox LB medium (Sigma-Aldrich) at 37 °C overnight under continuous stirring. Afterwards, 50 μl of the resulting turbid solution was added to 100 ml of fresh LB broth medium and harvested at the exponential growth phase evaluated using OD (optical density) and a standard reference growth curve, at a concentration of $10^7$ bacterial cells per mL. Then, the cells were diluted in phosphate buffered saline (PBS, Sigma-Aldrich, pH 7.2) to obtain a concentration of $10^5$ bacterial cells per mL. The scaffolds were placed in a 48-well plate and 50 μl of bacteria ($10^5$ CFU $ml^{-1}$) were dispersed over each scaffold. Afterwards, the scaffolds were incubated at 37 °C for 1 h. Subsequently, 150 μl of PBS was added to all wells, while half of the scaffolds were irradiated with NIR light at power densities of 1.39 W and 1.61 W $cm^{-2}$ for PLGA only and PLGA containing GO, MX and TMDCs, respectively, to achieve the same

 

temperature for each scaffold during an exposure time of 180 s. Colony forming units (CFUs) were evaluated after washing the scaffolds with PBS to harvest bacteria using LB agar plates incubated overnight at 37 °C. The number of CFUs was counted using FIJI software and the survival rate was expressed as a percentage compared to the control samples (PLGA).

### Statistical analysis

The obtained data are representative of at least three independent experiments. For all tests on cancer cell lines, one-way ANOVA and Turkey *post-hoc* tests were used. A $p$ value lower than 0.05 was considered statistically significant.

## Results and discussion

### Characterization of the initial nanomaterials

The overall quality, morphology and structure of all initial nanomaterials were assessed by electron microscopy, X-ray diffraction and Raman spectroscopy, as presented in Fig. 1.

Based on the transmission electron micrograph of GO (Fig. 1a), a typical 2D sheet-like structure with feature sizes in the micrometer range and variable transparency can be observed. This can be well connected with the multi-layer nature of the synthesized GO. XRD analysis (Fig. 1d) also confirms the quality of the produced GO with an interlayer distance of 0.75 nm based on the (001) diffraction point, which aligns well with state-of-the-art literature.[13] The obtained Raman spectrum of GO (Fig. 1g) displays the characteristic D (1347 $cm^{-1}$) and G (1591 $cm^{-1}$) peaks of GO with an ID/IG ratio of 1.05, which confirms the formation of GO using the conventional Hummers method.[32,33] The scanning electron micrograph of MX (Fig. 1b) verified the typical accordion-like structure, which is commonly observed for multi-layer $Ti_3C_2T_x$ nano-sheets. The measured diffractogram (Fig. 1e) confirmed the main diffraction peaks for $Ti_3C_2T_x$, which confirm their 2D structure, as well as an interlayer spacing of 0.87 nm, which agrees well with published literature data.[5,34] The Raman spectrum of the as-synthesized MX (Fig. 1h) depicts the characteristic MXene peaks located at 125, 212, and 701 $cm^{-1}$, as well as broader Raman peaks at around 285, 376, and 600 $cm^{-1}$. These peaks match well with contributions stemming from $Ti_3C_2O_2$, $Ti_3C_2F_2$, and $Ti_3C_2(OH)_2$.[35,36] The scanning electron micrographs and X-ray analysis of the TMDC (Fig. 1c and f) also confirmed their crystalline nature and plane, layered-like structure with flake sizes on the order of tens of micrometers. The obtained interlayer distance based on the (001) peak of 0.57 nm correlates well with the published data in the literature.[37] In the Raman spectrum of the TMDC (Fig. 1i), pronounced peaks are located at 223, 330 and 379 $cm^{-1}$, which align well with the commonly observed Raman signature for this TMDC.[37]

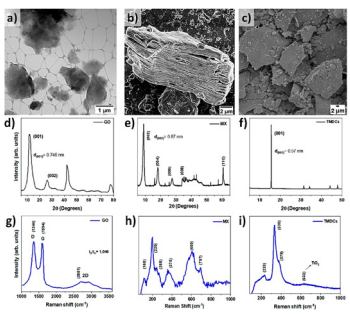

Fig. 1 Morphological and structural characterization of the initial (a, d and g) GO, (b, e and h) MX and (c, f and i) TMDC nano-materials by (a–c) electron microscopy, (d–f) X-ray diffraction and (g–i) Raman spectroscopy, respectively.

### Functional characterization of 3D-printed scaffolds

All PLGA scaffolds were 3D-printed through an extrusion-based technique. The used nanomaterials (GO, MX and TMCDs) are widely known for their photothermal conversion properties. Therefore, we assessed the temperature increase resulting from NIR irradiation using a laser with a wavelength of 808 nm in a time span of 180 seconds. We adjusted the laser power density for each scaffold to allow for a relative temperature increase of 45 °C, corresponding to a mild photothermal range (Fig. 2a and b). The PLGA–GO, PLGA–MX and PLGA–TMDC scaffolds were irradiated with different power densities to achieve a temperature increase up to 45 °C. Our evidence verified the high photothermal conversion properties of these nanomaterials, highlighting their feasibility for a PTT approach.

To infer the laser-induced heat diffusion from the scaffold to the tumor model, we designed a simulated framework in COMSOL Multiphysics to solve the heat-conduction equation (Fick's law). An illustration of the simulation framework consisting of a PLGA–GO disk as the scaffold, a hydrogel-based dome and the surrounding culture medium is depicted in Fig. 2c. Fig. 2d shows the isothermal curves evaluated in the $y$ = 0 plane after 180 s of laser irradiation. Laser irradiation gave rise to a relatively smooth temperature gradient over the dome (from 46 °C near the scaffold to 42 °C in the apical region, *ca.* 2.0 °C $mm^{-1}$), being a crucial aspect to equalize and maximize the biological effectiveness over the whole tumor region during the laser treatment. Another critical aspect to consider in this type of treatment is that the nanomaterials composing the scaffolds (GO, MX, and TMDCs) are also known to be photosensitizing agents. This implies that they can convert incident radiation into the production of radical species. Given their dual capabilities in photothermal conversion and radical generation, it is essential to investigate the photodynamic properties of these scaffolds. This dual functionality can enhance therapeutic outcomes by combining PTT with PDT, leveraging the generation of radical species under NIR irradiation.

Therefore, we further explored the photodynamic effects of these materials by assessing the generation of ROS upon NIR irradiation, providing a comprehensive understanding of their potential for combined PTT and PDT applications. For this purpose, we used the ROS-ID detection kit, which includes two

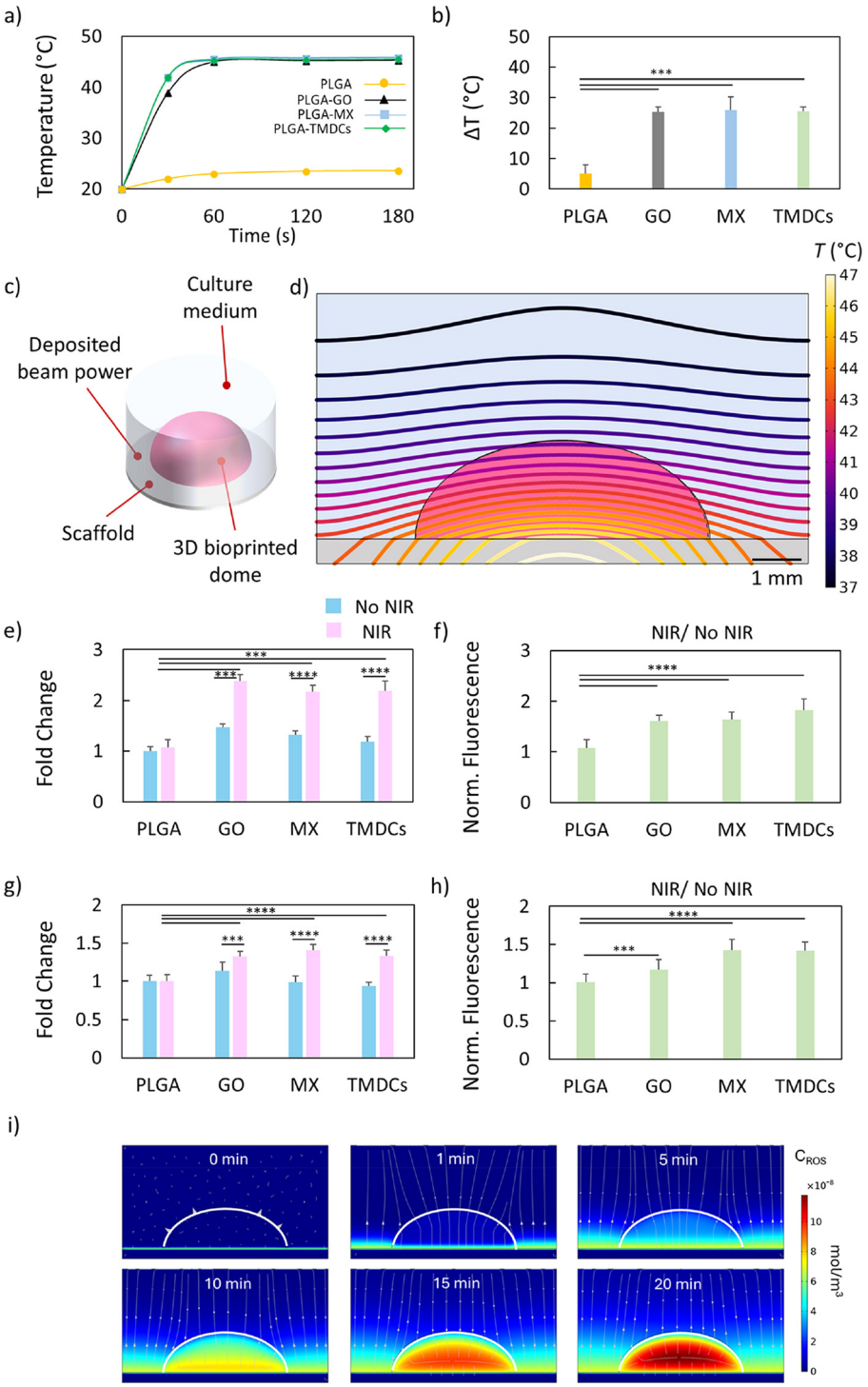


**Fig. 2** Photothermal and photodynamic conversion of the 3D-printed scaffolds. (a and b) Photothermal conversion of all scaffolds under NIR irradiation using a laser with a wavelength of 808 nm for 180 s at different power densities to achieve the same temperature increase. (c) Illustration of the simulation framework consisting of a PLGA–GO scaffold, a hydrogel-based dome and the surrounding culture medium. (d) Isothermal curves evaluated in the $y$ = 0 plane after 180 s of laser irradiation. (e) Fluorescence intensity of the green probe to detect oxidative stress. The results are expressed as fold change over non-irradiated PLGA. (f) Ratio between the green fluorescence intensity of the irradiated scaffolds and that of the non-irradiated ones. (g) Fluorescence intensity of the orange probe to detect superoxide radicals. The results are expressed as fold change over non-irradiated PLGA. (h) Ratio between the orange fluorescence intensity of the irradiated scaffolds and that of the non-irradiated ones. (i) Theoretical simulation of ROS distribution through the bioprinted model, reaching the whole structure in a time span of 20 minutes. *** $p < 0.001$; *** $p < 0.0001$; one-way ANOVA and Tukey *post-hoc* test.

probes to directly monitor the generation of reactive oxygen (green fluorescent probe) and/or superoxide species (orange fluorescent probe) in real time. We monitored the increase in fluorescence intensity due to ROS generation coming directly from the scaffolds without cells. After NIR radiation, we monitored the increase in the resulting fluorescence intensity of both probes (Fig. 2e–h). The fluorescence intensity of the green probe showed a notably increased production of general ROS with respect to PLGA and for all irradiated 3D-printed scaffolds (Fig. 2e). To quantify the ROS increase under NIR irradiation, we reported the ratio for each scaffold between the irradiated and not irradiated ones (Fig. 2f). Despite a small presence of free radicals produced by PLGA–GO without irradiation, all scaffolds showed a significant increase in green fluorescence with respect to their non-irradiated counterparts. We also monitored the generation of superoxide species using the orange fluorescent probe (Fig. 2g and h). A strong increase in fluorescence intensity, expressed as fold change over PLGA, was observed for all scaffolds, which aligns well with the findings for the green probe (Fig. 2g). The efficiency for superoxide generation was similarly calculated by reporting the ratio between the fluorescence intensities of the irradiated scaffolds and the non-irradiated ones (Fig. 2h). Overall, the 3D-printed scaffolds demonstrated exceptional photothermal conversion properties, along with the capability to act as photosensitizing agents through significant increases in ROS and superoxide generation under NIR irradiation. The dual functionality of these scaffolds in both PTT and PDT enhances their therapeutic potential, providing a synergistic approach for cancer treatment. Building on our initial observations of ROS generation under NIR irradiation, we sought to investigate the mechanism of action of ROS. The simulation demonstrated a rapid and uniform diffusion of ROS throughout the bioprinted tumor model through as a first-order reaction mechanism. After just 20 minutes, ROS concentrations reached equilibrium, with complete penetration into the hydrogel scaffold and cellular regions (Fig. 2i). This was evident in the ROS concentration heatmaps, which showed no significant spatial gradients, indicating a homogeneous distribution of ROS across the construct. The simulation quantified ROS concentrations across the bioprinted model, revealing that equilibrium was achieved within 20 minutes, regardless of initial ROS generation sites. This suggests that the dual functionality of the 3D-printed scaffolds—acting as both photothermal agents and photosensitizers—can efficiently deliver ROS to target regions under NIR irradiation. Our findings support the hypothesis that the photodynamic properties of the nanomaterials within the scaffolds play a crucial role in enhancing therapeutic outcomes. This comprehensive understanding underscores the potential of these scaffolds in synergistic PTT and PDT cancer therapies.

### Photothermal/photodynamic therapy through scaffolds on 3D-bioprinted breast cancer models

Our primary objective was to explore the biological effect of photothermal and photodynamic therapy on a complex biological model, the 3D-bioprinted breast tumor. In this setup, we evaluated the effect of the photothermal and photodynamic conversion efficiency of the 3D-printed scaffolds (Fig. 3a). For this purpose, we irradiated the scaffolds with an 808 nm laser at a specific power density calibrated for each material to reach 45 °C in 3 minutes (see the Experimental section) to subsequently evaluate their biological effect. The respective results are summarized in Fig. 3b. Initially, we evaluated the effects of NIR on the resulting cell viability. 3D-bioprinted breast cancer models did not suffer from a reduction in cell viability when in contact with PLGA alone or PLGA irradiated with NIR light. Moreover, the 3D-bioprinted cancer models in contact with PLGA–GO, PLGA–MX and PLGA–TMDCs did not show any significant difference in terms of viability with respect to the control sample. In contrast, upon NIR irradiation, we observed a notable reduction in the viability for the bioprinted cancer in contact with all scaffolds. In particular, the PLGA–TMDCs exhibited the highest anti-proliferative effects on HCC-1806 cells, decreasing viability to 47.9%. The reduction in viability caused by the irradiated PLGA–TMDCs was followed by the PLGA–MX scaffolds, which caused a decrease in viability to 64.7%. Therefore, we further investigated whether this strong reduction in viability is related to a high production in ROS. The results of ROS production under NIR radiation are shown in Fig. 3c and reported as fold change. All irradiated scaffolds caused a significant stimulation of oxidative stress with respect to the control group (PLGA only). As for the reduction in viability, the highest effect was observed for the PLGA–TMDC scaffolds, which showed a 3.5 times increased ROS production with respect to PLGA. This increase was followed by the PLGA–MX and PLGA–GO scaffolds, which caused an increase of 2.3- and 2.1-fold, respectively. These results are clearly indicative of a photodynamic-dependent anti-tumor effect. It has been reported in the literature that there is a strong correlation between ROS production and activation of autophagy.[38,39] Autophagy is a cellular degradation process that removes damaged organelles, misfolded proteins, and other cellular components to maintain cellular health. Oxidative stress induced by PDT can trigger autophagy as a protective mechanism to remove damaged cellular components and maintain cell viability.[40–42] However, excess autophagy may also contribute to cell death following PDT treatment.[43–45] To test the cellular response to the enhanced ROS production after PTT/PDT, we measured the formation of the autophagosome through a specific autophagosome detection kit (Fig. 3d and e). We observed a significant increase in autophagosome formation in terms of fold change after NIR radiation for the PLGA–GO, PLGA–MX and PLGA–TMDC scaffolds. The obtained results align well with the respective ROS production, highlighting the interplay between both mechanisms. In particular, the PLGA–MX and PLGA–TMDC scaffolds under NIR caused the highest increase in autophagosome detection, which resulted in 4.9 and 6.8 times higher values compared to the value detected for the 3D-bioprinted breast cancer in contact with PLGA only. Our findings provide compelling evidence of the synergistic relationship

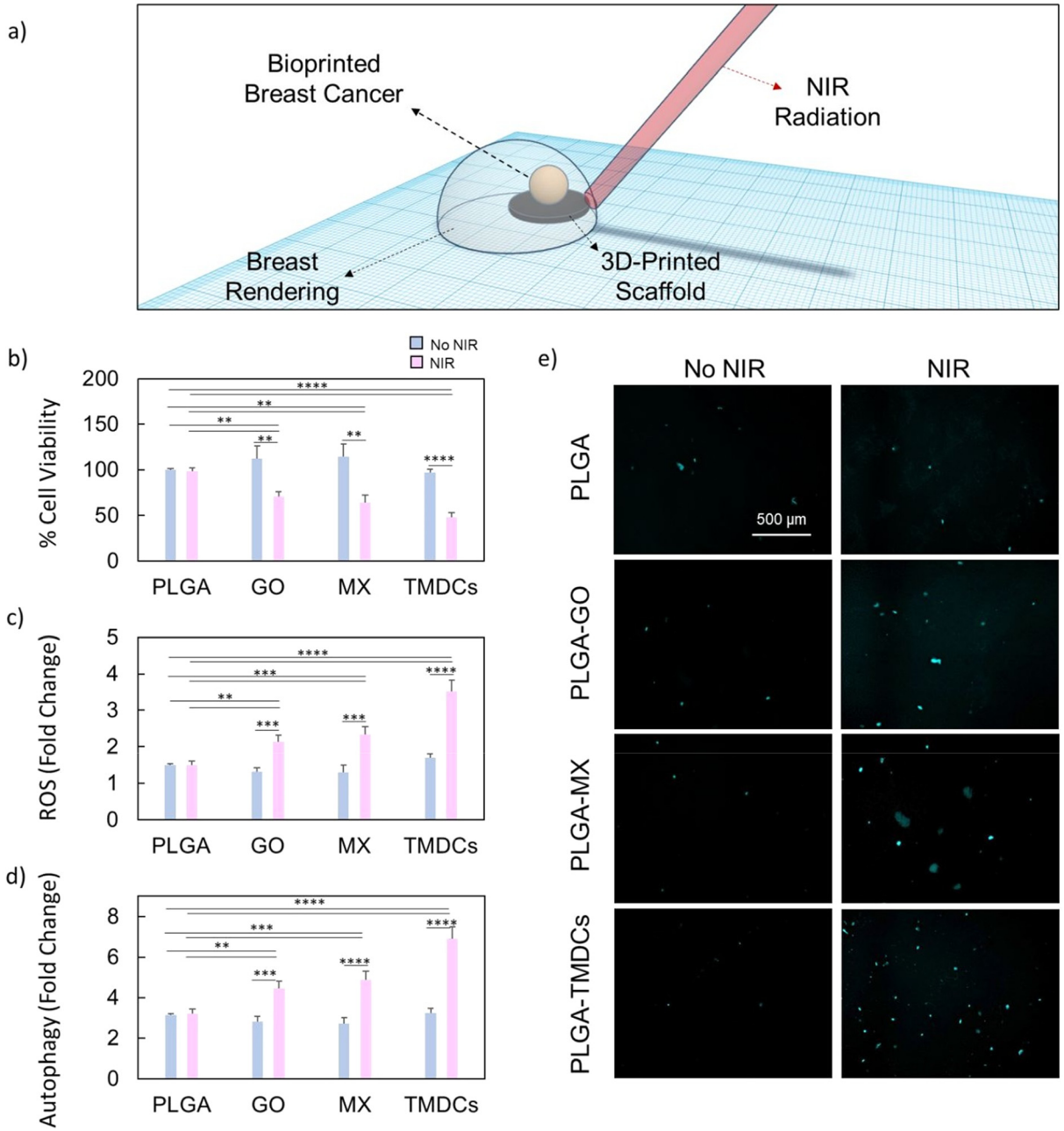


**Fig. 3** Biological effect of the photothermal/photodynamic therapy on 3D-bioprinted breast cancer models. (a) Schematic representation of the experimental setup, showing a rendering of the irradiated 3D-printed scaffolds in contact with the 3D-bioprinted breast cancer model. (b) Cell viability of the breast cancer model after NIR radiation on the 3D-printed scaffolds. The results are expressed as % of control breast cancer. (c) Production of reactive oxygen species after NIR radiation. The results are expressed as fold change. (d and e) Induction of the production of the autophagosome after NIR radiation and representative fluorescence images. The results are reported as fold change. * $p < 0.05$; ** $p < 0.01$; *** $p < 0.001$; **** $p < 0.0001$; one-way ANOVA and Tukey *post-hoc* test.

between ROS production, cellular cytotoxicity, and autophagy activation in response to PTT/PDT-mediated treatment. In combination with our previous results on the different adhesion propensions of the cells, we further highlight the potential of our 3D-printed scaffolds as promising candidates for highly selective anti-tumoral efficacy in breast cancer therapy.

### Induction of pyroptosis through photothermal/photodynamic therapy

Recent experimental evidence suggests a complex interplay between autophagy and pyroptosis, two distinct yet interconnected cellular processes.[38,39,46] Pyroptosis, unlike autophagy, is a form of programmed cell death that is inherently inflam-

 

matory and occurs through the activation of caspase-1 and gasdermin D (GSDMD), leading to cell lysis and the release of pro-inflammatory cytokines.[47,48] This process serves as a signal to recruit immune responses to the site of infection or tumorigenesis.[49–51] Given the contrast between the primarily survival-oriented process of autophagy and the destructive nature of pyroptosis, understanding the relationship between both processes could have profound implications for cancer therapy.[52–54]

Autophagy plays a crucial role in cellular homeostasis and stress adaptation, acting as a mechanism for recycling damaged organelles and macromolecules to sustain energy production and survival under adverse conditions. In the context of cancer, autophagy can promote tumor survival by mitigating cellular stress.[53] Importantly, autophagy has been shown to intersect with pyroptotic pathways, potentially modulating the extent and onset of inflammatory cell death.[54] The observed variation in autophagy levels, particularly its increase, might act as a protective cellular mechanism by delaying or suppressing pyroptosis, thereby offering cells a temporary reprieve from immune-mediated destruction. This hypothesis aligns with recent insights into a regulatory axis between autophagy and pyroptosis, where cells dynamically balance survival and inflammatory death under stress or damage. Such a balance is especially critical in the tumor microenvironment, where autophagy may serve to shield cancer cells from immune surveillance while pyroptosis could enhance anti-tumor immune responses.

For this purpose, we tested the expression of GSDMD on bioprinted breast cancer models after NIR radiation of the scaffolds (Fig. 4). Among the tested scaffolds, PLGA–GO demonstrated the highest induction of pyroptosis, followed by PLGA–TMDCs and PLGA–MX, when compared to the control PLGA scaffold (Fig. 4a). To quantify the tendency of the irradiated scaffolds to induce pyroptosis, we evaluated the efficiency, expressed as the ratio between the expression of GSDMD of the irradiated samples and the non-irradiated ones (Fig. 4b). The induction efficiency of pyroptosis indicated the tendency of PLGA–GO to induce this type of immunogenic cell death when compared to the other scaffolds. Importantly, we observed an inverse correlation between the levels of autophagy and pyroptosis. The scaffolds inducing higher levels of pyroptosis (notably PLGA–GO) correspondingly showed reduced signs of autophagy when compared to PLGA–MX and PLGA–TMDCs (Fig. 4c). This was evaluated by comparing the efficiency of the induction of pyroptosis with the efficiency of induction of autophagy. These findings align with the hypothesis that the stress responses elicited by higher pyroptosis rates can downregulate autophagy, further indicating a tightly regulated balance between both processes in the cellular response to NIR-induced stress. The differential induction of stress response pathways by various scaffold compositions presents a novel avenue for targeted cancer therapies. By selecting appropriate scaffold materials and NIR conditions, it will become possible to tailor the cellular response towards either a more conservative (autophagy) or a more immunogenic (pyroptosis) response.

### Migration of immune cells

The interaction between the immune system and the tumor microenvironment is crucial for an effective cancer therapy.[55,56] Therefore, we evaluated the migration of immune cells towards the cancer region after NIR irradiation using a transwell system (Fig. 5a). We first irradiated the 3D-printed scaffolds in contact with the bioprinted breast cancer models. After irradiation, we removed the supernatant and added it on

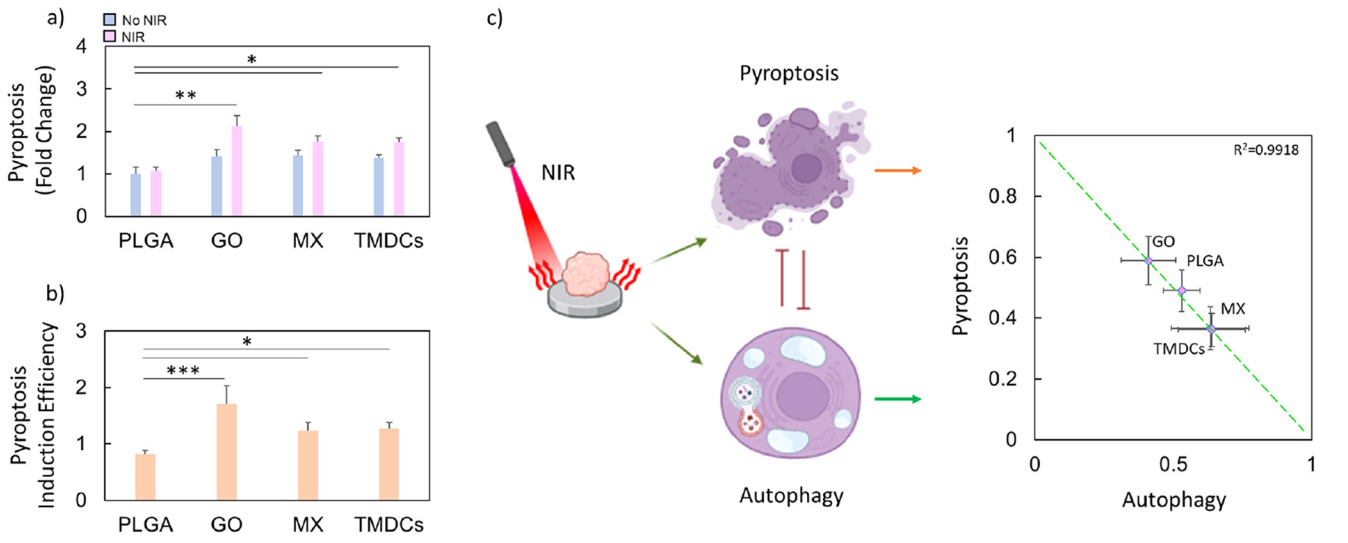


**Fig. 4** Pyroptosis induction after NIR radiation. (a) Induction of pyroptosis on bioprinted breast cancer models after NIR radiation of the scaffolds. The results are expressed as fold change of the PLGA scaffolds. (b) Efficiency of pyroptosis induction expressed as the ratio between the irradiated and non-irradiated samples. (c) Schematic illustration highlighting the inverse correlation between autophagy and pyroptosis as the ratio of pyroptotic or autophagic behaviour for each irradiated sample. * $p < 0.05$; ** $p < 0.01$; *** $p < 0.001$; one-way ANOVA and Tukey *post-hoc* test.

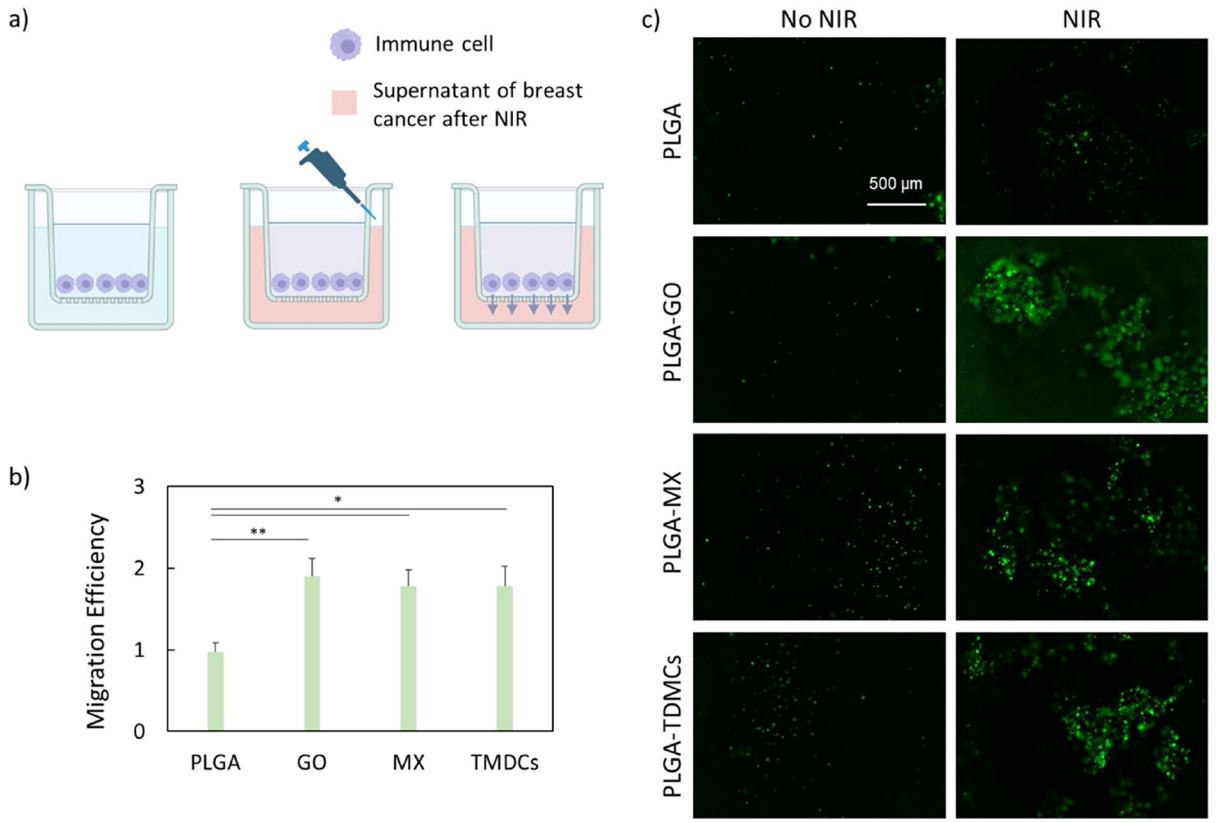


**Fig. 5** Migration of immune cells towards the cancer region after NIR irradiation. (a) Schematic representation of the transwell system used. (b) Migration efficiency expressed as the ratio between the fluorescence intensities of immune cells under non-irradiated conditions and immune cells under irradiated ones. (c) Representative images of the stained immune cells after migration in the lower chamber of the ttranswell. * $p < 0.05$; ** $p < 0.01$; one-way ANOVA and Tukey *post-hoc* test.

the lower chamber of the transwell. Subsequently, we seeded immune cells on the upper chamber, and evaluated the migration through calcein staining. The observed results are collectively summarized in Fig. 5b and c. After 24 hours of incubation, a significant migration of immune cells towards the cancer region was observed. Measurements of the migration efficiency demonstrated that the irradiated PLGA–GO, PLGA–MX and PLGA–TMDC scaffolds caused a notable increase in the migration of immune cells towards the cancer region (Fig. 5b), as highlighted by the representative images (Fig. 5c). Notably, the irradiated PLGA–GO scaffolds caused a higher migration of immune cells compared to the other scaffolds, confirming our hypothesis that immune cells tend to migrate more extensively towards cancer models showing higher pyroptosis levels. The observed recruitment of immune cells towards the cancer region underscores the potential of our 3D-printed scaffolds in enhancing anti-tumor immune response. The ability of the PLGA–GO, PLGA–MX, and PLGA–TMDC scaffolds to generate localized heat and ROS under NIR irradiation does not only directly damage cancer cells but also contributes to create a controlled inflammatory environment that attracts immune cells. This dual mechanism can potentiate the overall therapeutic efficacy by promoting tumor destruction through both direct cytotoxic effects and immune-mediated responses.

### Antibacterial activity of irradiated scaffolds

The antibacterial effect of the scaffolds is a necessity for successful clinical applications. By preventing infections, reducing antibiotic reliance, and fostering tissue integration, these scaffolds significantly enhance the efficacy and safety of regenerative medicine and tissue engineering approaches. To investigate the antibacterial effects of all scaffolds, the CFUs were calculated for *E. coli* and *S. aureus* with and without NIR irradiation, respectively, after an incubation time of 1 h. The results are presented in Fig. 6a (*E. coli*) and Fig. 6b (*S. aureus*) as a percentage compared to the control unit (PLGA only). The results indicate that without NIR radiation, the % CFUs of both *E. coli* and *S. aureus* treated with PLGA–GO decreased compared to the control. Without NIR irradiation, PLGA–MX exhibited an antibacterial effect (~50%) against *E. coli*, and showed no notable effect against *S. aureus*. The PLGA–TMDC scaffolds exhibited a negligible antibacterial effect against both species without NIR irradiation. After 180 s of NIR irradiation, the % CFUs for both *E. coli* and *S. aureus* decreased for all scaffolds compared to the non-irradiated

 

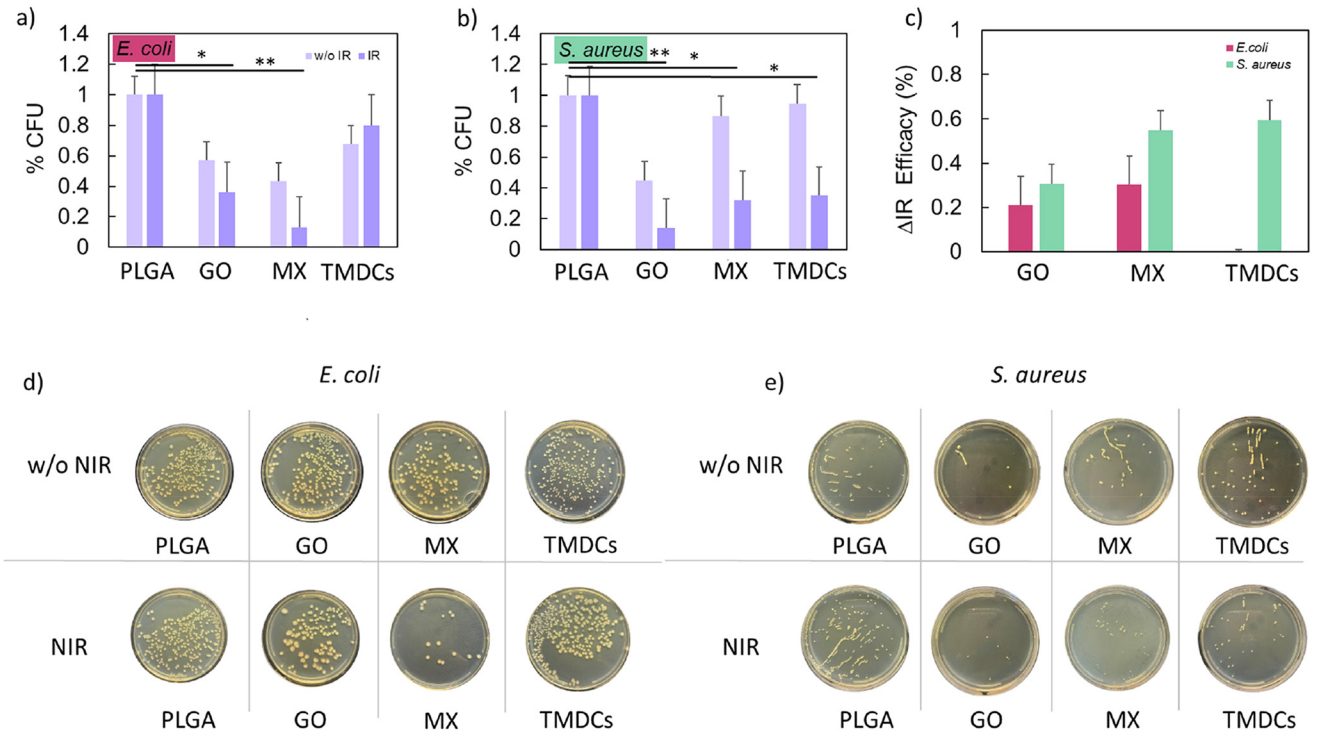


**Fig. 6** Antibacterial effect of the NIR treatment on the 3D-printed scaffolds. (a and b) CFUs calculated for *E. coli* and *S. aureus*, respectively, with and without NIR irradiation after an incubation time of 1 h. The values are normalized to the control scaffold. (c) Percentage of efficacy of NIR treatment for different scaffolds calculated as the relative difference between the irradiated and non-irradiated scaffolds. (d and e) Representative images of CFU plates for each sample with and without NIR irradiation for *E. coli* and *S. aureus*, respectively. * $p < 0.05$; ** $p < 0.01$; one-way ANOVA and Tukey *post-hoc* test.

samples except for the PLGA–TMDC scaffolds, which did not exhibit an antibacterial effect against *E. coli* even under elevated temperature conditions. The antibacterial effect appears to be higher when using the NIR-irradiated PLGA–MX scaffolds in the case of *E. coli* (Fig. 6a), while the NIR-irradiated PLGA–GO scaffolds showed the highest antibacterial effect against *S. aureus* (Fig. 6b). Representative images of CFU plates for each sample are presented in Fig. 6d and e, whereas Fig. 6c summarizes the % efficacy of NIR irradiation for all materials. PLGA–GO and PLGA–MX showed a higher % efficacy compared to PLGA–TMDCs in the case of *E. coli*, with a relative improvement of the antibacterial effect of ~20 and 30%, respectively, upon NIR treatment. However, an opposite trend can be observed for *S. aureus*, for which PLGA–TMDC and PLGA–MX exhibited a higher % efficacy compared to PLGA–GO, with a more than ~60% improvement after NIR irradiation. We hypothesize that the different results against the two species can be ascribed to their specific sensitivity to external stress. Indeed, from previous studies, *E. coli* has been demonstrated to be more sensitive to ROS species,[57] whereas *S. aureus* is known to be more susceptible to high temperatures (>40 °C).[58] These outcomes can be explained considering the different biochemical compositions of Gram-positive and Gram-negative bacteria's outer structures.[59] The Gram-negative, *i.e. E. coli*, cell wall is made up of the cytoplasmatic membrane, followed by a periplasmatic space, a peptidoglycan layer, the outer membrane, and a lipopolysaccharide layer (from the inner part to the outer part). In contrast, the Gram-positive, *i.e. S. aureus*, cell wall is composed of the cytoplasmatic membrane followed by a peptidoglycan layer. The most relevant layers that are crucial to defend bacteria from ROS species have proved to be the lipopolysaccharide and the peptidoglycan layers. In fact, the peptidoglycan layer in Gram-positive bacteria is known to act as a barrier for ROS species produced in the external environment. In contrast, the lipopolysaccharide barrier of Gram-negative bacteria displayed a higher susceptibility to ROS, since singlet oxygen ($O^{\bullet -}$) might initiate radical chain reactions that result in the production of endogenous ROS species.

### Biocompatibility and adhesion on 3D-printed scaffolds

A crucial aspect following tumor ablation *via* PTT and PDT is the possibility of tissue regeneration. It has been widely shown that certain nanomaterials under the right conditions can promote tissue regeneration and thus serve both as photoactivators to reduce the tumor mass and as promoters in regenerative medicine.[60–63] We seeded three different cell lines on the scaffolds to verify adhesion and metabolic activity (Fig. 7). In this setup, we investigated the differences in terms of viability and adhesion between breast cancer cells and two non-tumor cell lines, *i.e.* fibroblasts and bone marrow mesenchymal stem cells. We quantified viability as the ratio of live to dead cells,

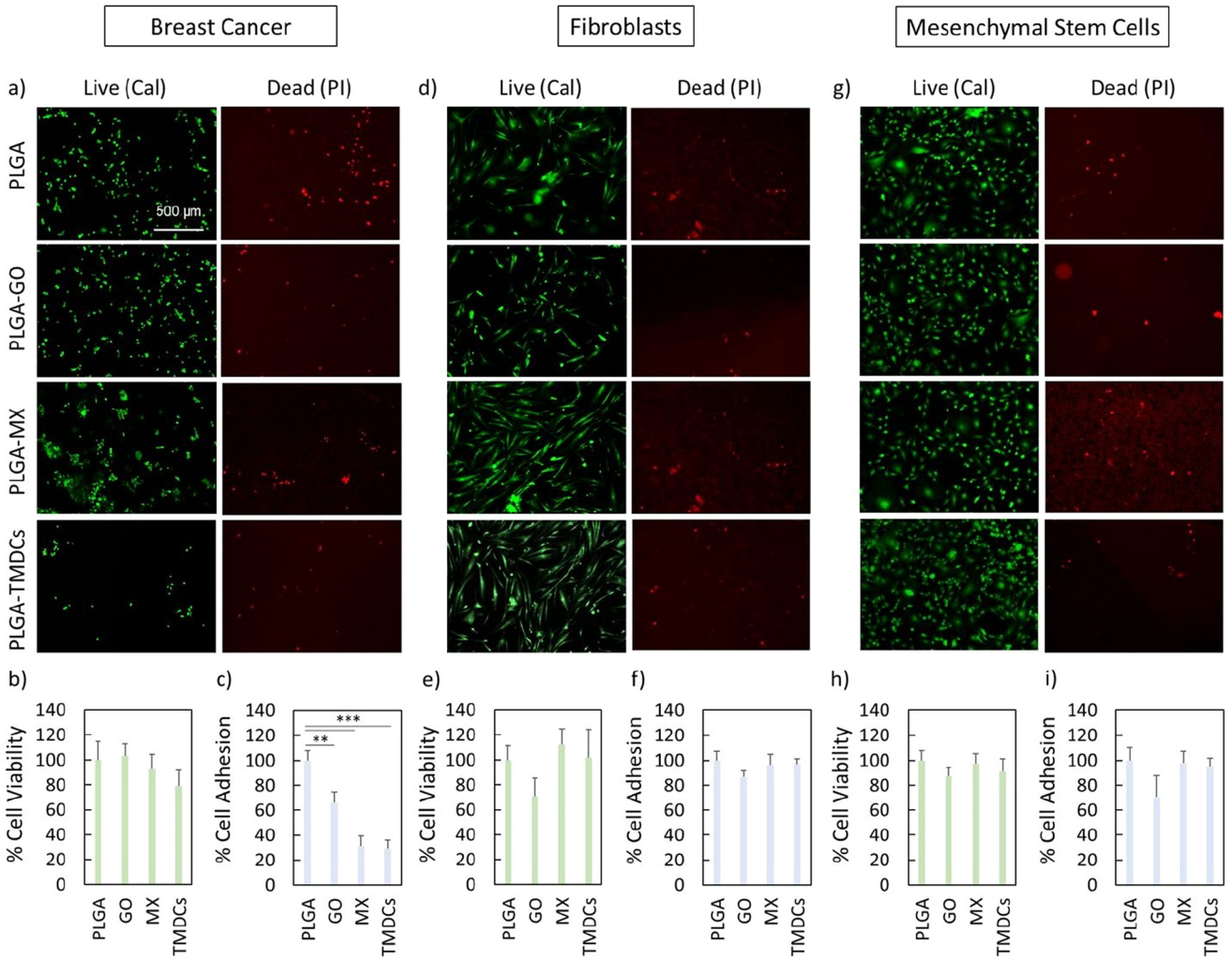


**Fig. 7** Biocompatibility of the 3D-printed scaffolds on human breast cancer cells, fibroblasts and mesenchymal stem cells. (a, d and g) Representative live/dead images of human breast cancer cells, human fibroblasts and mesenchymal stem cells, respectively. (b, e and h) Cell viability of human breast cancer cells, human fibroblasts and mesenchymal stem cells seeded on the 3D-printed discs, respectively. The results are reported as % of control (PLGA). (c, f and i) Cell adhesion of human breast cancer cells, human fibroblasts and mesenchymal stem cells on the 3D-printed scaffolds, respectively. The results are reported as % of control (PLGA). (f) Cell adhesion of human fibroblasts on the 3D-printed scaffolds. ** $p < 0.01$; *** $p < 0.001$; one-way ANOVA and Tukey *post-hoc* test.

normalized to values obtained with PLGA scaffolds. Representative images of live and dead cells are presented in Fig. 7a, d and g, where live cells are stained in green with calcein and dead cells are stained in red with propidium iodide.

Notably, the scaffolds did not exhibit cytotoxicity (viability >70%) for all the cells used (Fig. 7b, e and h). Interestingly, the adhesion behavior of human breast cancer cells was significantly influenced by the scaffold materials (Fig. 7c). In contrast, human fibroblasts and mesenchymal stem cells exhibited consistent adhesion regardless of scaffold type (Fig. 7f and i).

These findings underscore a crucial aspect in the realm of regenerative medicine, highlighting the potential of scaffold materials in guiding cell behavior. In summary, our data underscore the potential of using nanomaterial-enriched 3D-printed scaffolds for dual anticancer and regenerative applications.[64] The minimal cytotoxicity observed with the MX and TMDC scaffolds towards breast cancer cells highlights their safety profile, whereas the differential adhesion patterns observed suggest that the scaffold material composition plays a crucial role in modulating cellular behavior. This study provides a foundation for the development of advanced scaffolds tailored for specific biomedical applications, combining tumor ablation with tissue regeneration, thus offering a promising avenue for future research and clinical translation.

## Conclusions

The study focused on the integration of PTT/PDT using 3D-printed scaffolds composed of PLGA together with 2D nanomaterials such as GO, MX and TMDCs on 3D-bioprinted

 

breast cancer models. A key strength of this research lies in the use of 3D-bioprinted breast cancer models, which resemble more accurately the tumor microenvironment and cellular architecture seen in clinical settings compared to traditional 2D culture systems. This advanced model enhances the clinical relevance of the findings and supports the potential for rapid translation of these therapeutic strategies into clinical applications. It allows culturing of cells derived from biopsies of patients, not having to deal with commercial cell lines or with the different physiologies of animal models, which has substantive differences.

Here we directly compared the effects of three 2D materials synthesized in the last 15 years and promising candidates for PDT/PTT *in vivo*. All the scaffolds demonstrated robust capabilities in both photothermal conversion and photodynamic processes, generating significant ROS upon NIR irradiation. This dual functionality led to pronounced biological effects, including oxidative stress, autophagy, and pyroptosis. Importantly, these effects were observed in a complex, 3D tumor model that closely mimics human breast cancer, underlining the potential of these scaffolds to achieve selective and effective cancer cell targeting in a realistic setting. Moreover, the ability of these scaffolds to induce specific cellular responses such as pyroptosis did not only highlight their potential to directly target and kill cancer cells but also suggested a mechanism for initiating an immune response, which is crucial for sustained cancer suppression and prevention of recurrence. The differential antibacterial activity further indicated the utility of these scaffolds after mastectomy, reducing infection risks.[65] A pivotal aspect of this research is the strategic use of these materials to tune the therapeutic outcomes, leveraging their unique properties for targeted cancer therapy. In this regard, GO scaffolds stood out for their notable induction of pyroptosis, which is highly inflammatory, thus effectively triggering immune responses. Interestingly, GO also showed reduced activation of autophagy compared to the other 2D materials, which positions it as particularly effective in initiating a stronger immune response due to its high immunogenicity. This capability makes GO an excellent candidate for therapies, for which enhanced immune activation is desired. In contrast, $TiS_2$ (member of the TMDC family) in the scaffolds was associated with a higher induction of ROS and increased autophagy. The marked ROS generation by TMDCs underscored their potential in creating a highly oxidative environment that can induce cancer cell death through oxidative stress. Simultaneously, the elevated autophagy suggests a dual role, where cells attempt to mitigate damage but can also succumb to autophagic cell death under persistent stress. These findings make TMDCs suitable for aggressive treatment approaches, for which both direct and collateral damage to tumor cells is beneficial. MX demonstrated a balanced effect between inducing pyroptosis and promoting autophagy with substantial ROS production. This balanced response positions MX as the most versatile material that can be tailored to achieve specific therapeutic outcomes, adaptable to different therapeutic needs and tumor types. MX's adaptability allows it to be tuned for either more conservative treatments *via* autophagy or more aggressive approaches *via* enhanced pyroptosis.

Finally, all scaffolds displayed promising regenerative medicine-oriented preliminary evidence, showing good cell adhesion of fibroblasts and mesenchymal stem cells compared to human breast cancer cells. Overall, this research did not only demonstrate the efficacy of using a 3D-bioprinted breast cancer model for more clinically relevant outcomes, but also highlighted how the choice of a specific 2D material can be strategically utilized to control and enhance the therapeutic response.

Consequently, by fine-tuning the scaffold nano-photoadsorbers, it is possible to direct the treatment pathway—whether to enhance the respective immune responses, increase oxidative stress, or balance between cellular death mechanisms according to patient requirement. In addition, scaffold shape can be tailored to adapt to the tumor model thereby ensuring homogeneous temperature distribution, and hence homogeneous treatment effectiveness, during scaffold irradiation. These promising results affirm the potential for these scaffold-based bioprinting technologies to revolutionize personalized cancer therapy, providing a platform for future studies to explore and optimize these interactions in clinical settings.

## Data availability

Data for this article are available on demand at **https://www.unicatt.it**.

## Conflicts of interest

The authors declare that they have no known competing financial interests or personal relationships that could have appeared to influence the work reported in this paper.

## Acknowledgements

A. Rosenkranz gratefully acknowledges the financial support from ANID-Chile within the projects Fondecyt Regular 1220331 and Fondequip EQM190057 as well as the Millennium Science Initiative Program ANID-Milenio (NCN2023_007). Moreover, A. Rosenkranz gratefully acknowledges Dr Simon Fleischmann (Helmholtz Institute Ulm (HIU) and Karlsruhe Institute of Technology (KIT)) for his kind support and supply of $TiS_2$. D. Zambrano acknowledges the financial support from ANID postdoctoral FONDECYT (3220165). The research leading to these results has received funding from AIRC under IG 2019—ID. 23124 project (PI Prof. Massimiliano Papi).

## References

1 H. Liu, *et al.* Advanced Nanomaterials in Medical 3D Printing, *Small Methods*, 2024, **8**, 2301121.
2 M. Overchuk, R. A. Weersink, B. C. Wilson and G. Zheng, Photodynamic and Photothermal Therapies: Synergy Opportunities for Nanomedicine, *ACS Nano*, 2023, **17**, 7979–8003.
3 H. S. Kim and D. Y. Lee, Near-infrared-responsive cancer photothermal and photodynamic therapy using gold nanoparticles, *Polymers*, 2018, **10**, 961.
4 M. Li, X. Yang, J. Ren, K. Qu and X. Qu, Using graphene oxide high near–infrared absorbance for photothermal treatment of Alzheimer's disease, *Adv. Mater.*, 2012, **24**, 1722–1728.
5 G. Perini, *et al.* Advanced usage of Ti3C2Tx MXenes for photothermal therapy on different 3D breast cancer models, *Biomed. Pharmacother.*, 2022, **153**, 113496.
6 A. Rosenkranz, *et al.* Laser-Mediated antibacterial effects of Few-and Multi-Layer Ti3C2Tx MXenes, *Appl. Surf. Sci.*, 2021, **567**, 150795.
7 Y. Zhao, S.-B. Wang, A.-Z. Chen and R. K. Kankala, Nanoarchitectured assembly and surface of two-dimensional (2D) transition metal dichalcogenides (TMDCs) for cancer therapy, *Coord. Chem. Rev.*, 2022, **472**, 214765.
8 V. Palmieri, F. Sciandra, M. Bozzi, M. De Spirito and M. Papi, 3D graphene scaffolds for skeletal muscle regeneration: future perspectives, *Front. Bioeng. Biotechnol.*, 2020, **8**, 00383.
9 V. Palmieri, *et al.* Graphene Oxide Nano-Concentrators Selectively Modulate RNA Trapping According to Metal Cations in Solution, *Front. Bioeng. Biotechnol.*, 2020, **8**, 421.
10 V. Palmieri, M. De Spirito and M. Papi, Graphene-based scaffolds for tissue engineering and photothermal therapy, *Nanomedicine*, 2020, **15**, 1411–1417.
11 L. Fusco, *et al.* Immune profiling and multiplexed label–free detection of 2D MXenes by mass cytometry and high–dimensional imaging, *Adv. Mater.*, 2022, **34**, 2205154.
12 L. Fusco, *et al.* Immune profiling and multiplexed label–free detection of 2D MXenes by mass cytometry and high–dimensional imaging, *Adv. Mater.*, 2022, **34**, 2205154.
13 G. Perini, *et al.* Slow and steady wins the race: Fractionated near-infrared treatment empowered by graphene-enhanced 3D scaffolds for precision oncology, *Mater. Today Bio*, 2024, **25**, 100986.
14 S. Liu, X. Pan and H. Liu, Two–dimensional nanomaterials for photothermal therapy, *Angew. Chem.*, 2020, **132**, 5943–5953.
15 G. Perini, V. Palmieri, G. Ciasca, M. De Spirito and M. Papi, Unravelling the Potential of Graphene Quantum Dots in Biomedicine and Neuroscience, *Int. J. Mol. Sci.*, 2020, **21**, 3712.
16 D. Zhi, T. Yang, J. O'hagan, S. Zhang and R. F. Donnelly, Photothermal therapy, *J. Controlled Release*, 2020, **325**, 52–71.
17 G. Perini, *et al.* Carboxylated graphene quantum dots-mediated photothermal therapy enhances drug-membrane permeability, ROS production, and the immune system recruitment on 3D glioblastoma models, *Cancer Nanotechnol.*, 2023, **14**, 13.
18 J. Usuda, *et al.* Photodynamic Therapy (PDT) for Lung Cancers, *J. Thorac. Oncol.*, 2006, **1**, 489–493.
19 A. Gazzi, *et al.* Photodynamic therapy based on graphene and MXene in cancer theranostics, *Front. Bioeng. Biotechnol.*, 2019, **7**, 295.
20 N. Tyagi, *et al.* Mechanism and potentialities of photothermal and photodynamic therapy of transition metal dichalcogenides (TMDCs) against cancer, *Luminescence*, 2024, **39**, e4770.
21 J. Kadkhoda, A. Tarighatnia, M. R. Tohidkia, N. D. Nader and A. Aghanejad, Photothermal therapy-mediated autophagy in breast cancer treatment: Progress and trends, *Life Sci.*, 2022, **298**, 120499.
22 M. Cheng, *et al.* Conceptualizing Scaffold Guided Breast Tissue Regeneration in a Preclinical Large Animal Model, *Bioengineering*, 2024, **11**, 593.
23 R. A. Karami, O. Abou Ghanem and A. E. Ibrahim, Radiotherapy and breast reconstruction: a narrative review, *Ann. Breast Surg.*, 2020, **4**, 17.
24 A. Hladnik, G. Krumpak, M. Debeljak and D. G. Svetec, Assessment of paper surface topography and print mottling by texture analysis. in *Proceedings of ImageJ User & Developer Conference*, Luxembourg 2010.
25 G. Friggeri, *et al.* Multifunctional scaffolds for biomedical applications: Crafting versatile solutions with polycaprolactone enriched by graphene oxide, *APL Bioeng.*, 2024, **8**, 016115.
26 E. Staderini, *et al.* Effects of Thermoforming on the Mechanical, Optical, Chemical, and Morphological Properties of PET-G: In Vitro Study, *Polymers*, 2024, **16**, 203.
27 M. Sharifi, *et al.* 3D bioprinting of engineered breast cancer constructs for personalized and targeted cancer therapy, *J. Controlled Release*, 2021, **333**, 91–106.
28 H. Lin, X. Wang, L. Yu, Y. Chen and J. Shi, Two-Dimensional Ultrathin MXene Ceramic Nanosheets for Photothermal Conversion, *Nano Lett.*, 2017, **17**, 384–391.
29 W. S. Hummers Jr. and R. E. Offeman, Preparation of Graphitic Oxide, *J. Am. Chem. Soc.*, 1958, **80**, 1339.
30 M. A. Rafiee, *et al.* Fracture and fatigue in graphene nanocomposites, *Small*, 2010, **6**, 179.
31 F. Wang, L. T. Drzal, Y. Qin and Z. Huang, Mechanical properties and thermal conductivity of graphene nanoplatelet/epoxy composites, *J. Mater. Sci.*, 2015, **50**, 1082–1093.
32 J. Chen, B. Yao, C. Li and G. Shi, An improved Hummers method for eco-friendly synthesis of graphene oxide, *Carbon*, 2013, **64**, 225–229.
33 L. Shahriary and A. A. Athawale, Graphene oxide synthesized by using modified hummers approach, *Int. J. Renew. Energy Environ. Res.*, 2014, **2**, 58–63.

 

34 A. Rosenkranz, *et al.* Laser-Mediated antibacterial effects of Few- and Multi-Layer Ti3C2Tx MXenes, *Appl. Surf. Sci.*, 2021, **567**, 150795.
35 K. Shevchuk, A. Sarycheva, C. E. Shuck and Y. Gogotsi, Raman Spectroscopy Characterization of 2D Carbide and Carbonitride MXenes, *Chem. Mater.*, 2023, **35**, 8239–8247.
36 A. Sarycheva and Y. Gogotsi, Raman spectroscopy analysis of the structure and surface chemistry of Ti3C2T x MXene, *Chem. Mater.*, 2020, **32**, 3480–3488.
37 S. Sharma, S. Singh, R. C. Singh and S. Sharma, Structural transformation and room temperature ammonia sensing properties of $TiS_2$ nanostructures, *SN Appl. Sci.*, 2020, **2**, 887.
38 R. Guo, H. Wang and N. Cui, Autophagy regulation on pyroptosis: mechanism and medical implication in sepsis, *Mediators Inflammation*, 2021, 9925059.
39 H. Zhao, H. Liu, Y. Yang and H. Wang, The role of autophagy and pyroptosis in liver disorders, *Int. J. Mol. Sci.*, 2022, **23**, 6208.
40 M. Dewaele, H. Maes and P. Agostinis, ROS-mediated mechanisms of autophagy stimulation and their relevance in cancer therapy, *Autophagy*, 2010, **6**, 838–854.
41 L. Li, J. Tan, Y. Miao, P. Lei and Q. Zhang, ROS and autophagy: interactions and molecular regulatory mechanisms, *Cell. Mol. Neurobiol.*, 2015, **35**, 615–621.
42 Y. Chen and S. B. Gibson, Is mitochondrial generation of reactive oxygen species a trigger for autophagy?, *Autophagy*, 2008, **4**, 246–248.
43 S. Shimizu, T. Yoshida, M. Tsujioka and S. Arakawa, Autophagic cell death and cancer, *Int. J. Mol. Sci.*, 2014, **15**, 3145–3153.
44 Y. Liu and B. Levine, Autosis and autophagic cell death: the dark side of autophagy, *Cell Death Differ.*, 2015, **22**, 367–376.
45 E. Tasdemir, *et al.* Methods for assessing autophagy and autophagic cell death, *Autophagosome and phagosome*, 2008, pp. 29–76.
46 B. G. Byrne, J.-F. Dubuisson, A. D. Joshi, J. J. Persson and M. S. Swanson, Inflammasome components coordinate autophagy and pyroptosis as macrophage responses to infection, *mBio*, 2013, **4**, 10–1128.
47 Q. Wei, R. Zhu, J. Zhu, R. Zhao and M. Li, E2-induced activation of the NLRP3 inflammasome triggers pyroptosis and inhibits autophagy in HCC cells, *Oncol. Res.*, 2019, **27**, 827.
48 L. Lin, *et al.* Autophagy, pyroptosis, and ferroptosis: new regulatory mechanisms for atherosclerosis, *Front. Cell Dev. Biol.*, 2022, **9**, 809955.
49 L. Li, *et al.* Pyroptosis, a new bridge to tumor immunity, *Cancer Sci.*, 2021, **112**, 3979–3994.
50 T. Du, *et al.* Pyroptosis, metabolism, and tumor immune microenvironment, *Clin. Transl. Med.*, 2021, **11**, e492.
51 R. Loveless, R. Bloomquist and Y. Teng, Pyroptosis at the forefront of anticancer immunity, *J. Exp. Clin. Cancer Res.*, 2021, **40**, 264.
52 J. Sun, J. S. Fleishman, X. Liu, H. Wang and L. Huo, Targeting novel regulated cell death: Ferroptosis, pyroptosis, and autophagy in sepsis-associated encephalopathy, *Biomed. Pharmacother.*, 2024, **174**, 116453.
53 Q. Sun, J. Fan, T. R. Billiar and M. J. Scott, Inflammasome and autophagy regulation: a two- way street, *Mol. Med.*, 2017, **23**, 188–195.
54 Q. Wei, R. Zhu, J. Zhu, R. Zhao and M. Li, E2-induced activation of the NLRP3 inflammasome triggers pyroptosis and inhibits autophagy in HCC cells, *Oncol. Res.*, 2019, **27**, 827.
55 J. Nam, *et al.* Chemo-photothermal therapy combination elicits anti-tumor immunity against advanced metastatic cancer, *Nat. Commun.*, 2018, **9**, 1074.
56 Q. Chen, *et al.* Photothermal therapy with immune-adjuvant nanoparticles together with checkpoint blockade for effective cancer immunotherapy, *Nat. Commun.*, 2016, **7**, 13193.
57 S. S. Yong, J. I. Lee and D. H. Kang, TiO2-based photocatalyst Generated Reactive Oxygen Species cause cell membrane disruption of Staphylococcus aureus and Escherichia coli O157:H7, *Food Microbiol.*, 2022, **109**, 104119.
58 A. E. Nabiilah, Y. Jiwintarum and E. Y. Tatontos, Effect of Temperature on Viability of Normal Flora Bacteria (Escherichia Coli and Staphylococcus Aureus), *Malays. J. Med. Health Sci.*, 2021, **17**, 44–47.
59 T. A. Dahl, W. R. Midden and P. E. Hartman, Comparison of killing of Gram-negative and Gram-positive bacteria by pure singlet oxygen, *J. Bacteriol.*, 1989, **171**, 2188–2194.
60 F. Tiberio, *et al.* The osteoconductive properties of graphene-based material surfaces are finely tuned by the conditioning layer and surface chemistry, *Mater. Adv.*, 2024, **5**, 4772–4785.
61 S. Verma, A. J. Domb and N. Kumar, Nanomaterials for regenerative medicine, *Nanomedicine*, 2011, **6**, 157–181.
62 E. I. Medina-Reyes, D. Garcia-Viacobo, F. A. Carrero-Martinez and Y. I. Chirino, Applications and risks of nanomaterials used in regenerative medicine, delivery systems, theranostics, and therapy, *Crit. Rev. Ther. Drug Carrier Syst.*, 2017, **34**, 35–61.
63 G. Perini, *et al.* Near-infrared controlled release of mesenchymal stem cells secretome from bioprinted graphene-based microbeads for nerve regeneration, *Int. J. Bioprinting*, 2023, **10**, 1045.
64 G. Perini, *et al.* Graphene Quantum Dots' Surface Chemistry Modulates the Sensitivity of Glioblastoma Cells to Chemotherapeutics, *Int. J. Mol. Sci.*, 2020, **21**, 6301.
65 V. Palmieri, *et al.* Reduction and shaping of graphene-oxide by laser-printing for controlled bone tissue regeneration and bacterial killing, *2D Mater.*, 2018, **5**, 15027.